Ultrafast interfacial charge transfer and superior photoelectric conversion properties in one-dimensional Janus-MoSSe/WSe_2 van der Waals heterostructures

Biao Cai,[1,*] Jianing Tan,[1,*] Long Zhang,[2,*] Degao Xu,[1] Jiansheng Dong,[3] and Gang Ouyang[1,†]

[1]*Key Laboratory of Low-Dimensional Quantum Structures and Quantum Control of Ministry of Education, Key Laboratory for Matter Microstructure and Function of Hunan Province, School of Physics and Electronics, Hunan Normal University, Changsha 410081, China*

[2]*Hunan Key Laboratory of Super Microstructure and Ultrafast Process, Hunan Key Laboratory of Nanophotonics and Devices, School of Physics and Electronics, Central South University, Changsha 410083, China*

[3]*Department of Physics, Jishou University, Jishou 416000, China*

(Received 25 March 2023; revised 15 June 2023; accepted 10 July 2023; published 24 July 2023)

One-dimensional (1D) van der Waals (vdW) heterostructures have attracted great attention due to their excellent photoelectric properties which potentially serve as key components for next-generation optoelectronic devices. However, investigations on the photoelectric conversion properties in 1D vdW heterostructures are still in the rudimentary stage. Addressing the mechanism of the role of flexoelectricity in nanotubes and electronegativity difference of Janus materials on photoelectric properties remains challenging. In this paper, we investigate the flexoelectric effect and electronegativity difference on the photoelectric properties of 1D Janus-MoSSe/WSe_2 vdW heterostructures and assess their potential for solar cells through the atomic-bond-relaxation approach combined with *ab initio* nonadiabatic molecular dynamics simulations. We find that a 1D MoSSe/WSe_2 vdW heterostructure with *AB*1 stacking configuration exhibits ultrafast interfacial charge transfer and superior photoelectric conversion properties owing to the beneficial effects of flexoelectricity and electronegativity difference. Specifically, the photogenerated electron (hole) transfer in the 1D MoSSe/WSe_2 system occurs quickly, within 55 (17) fs. Moreover, the optimal power conversion efficiency of 1D MoSSe/WSe_2 vdW heterostructure-based solar cells can reach up to 6.25%, which is significantly higher than those of 1D MoS_2/WSe_2 (5.45%) and 2D MoSSe/WSe_2 (1.94%). In this paper, we provide an effective strategy for the development of high-efficiency solar cells.

DOI: 10.1103/PhysRevB.108.045416

I. INTRODUCTION

Two-dimensional transition metal dichalcogenides (2D-TMDs) and associated van der Waals (vdW) heterostructures have attracted tremendous interest because of their unique optoelectronic properties which have extensive applications in photodetectors, LEDs, and new-generation solar cells [1–3]. It has been reported that 2D-TMDs exhibit strong light-matter interaction and superior light absorption ability in the visible light region [4,5]. Additionally, the dissociation of photogenerated electron-hole pairs and restrained interlayer recombination can be accelerated due to a staggered type-II band alignment in the TMD heterostructures [6,7]. However, the power conversion efficiency (PCE) of TMD heterostructure-based solar cells is limited to the range of 0.2–1.7% due to carriers being confined in the 2D plane, which is still far below the Shockley-Queisser limit of 33% [8–11].

Recently, 2D Janus TMDs (e.g., MoSSe, WSSe) have received great attention due to their unique physical and chemical properties induced by structural asymmetry [12,13]. This type of TMD not only retains the normal advantages of pristine TMDs, such as tunable band gap, high absorption coefficient, and short carrier migration distance, but also possesses an intrinsic out-of-plane electric field induced by electronegativity difference between the chalcogens, which is expected to suppress carrier recombination and achieve excellent photoelectric performance [14–16]. Additionally, their corresponding one-dimensional (1D) systems such as nanotubes (NTs) and 1D vdW heterostructures have been demonstrated as promising nanostructures for application in nano-optoelectronic devices [17,18]. For example, the bent TMDs exhibit an out-of-plane spontaneous flexoelectric effect induced by strain gradient. As a result, an ultrafast electron-hole dissociation was achieved [19–21]. Zhang *et al.* [17] reported a giant bulk photovoltaic effect in WS_2 NTs and found that the photocurrent density is 2–6 orders of magnitude larger than ferroelectric bulk materials. Recently, 1D TMD-based radial vdW heterostructures have been successfully fabricated in experiment [18,22–26]. Burdanova *et al.* [22,23] showed a 1D C/BN/MoS_2 vdW heterostructure with high carrier mobility and demonstrated that it has a superior absorbance in comparison with a 1D C/BN heterostructure in the range of the visible light region. Very recently, Ghosh *et al.* [26] found that the photocurrent in a 1D MoS_2/WS_2 vdW heterostructure is threefold greater than 2D planar counterparts due to the photoconfinement effect of 1D hetero-NTs. Moreover, 1D TMD-based heterostructures with type-II band alignment exhibit ultrafast interfacial charge transfer, which

*These authors contributed equally to this work.
†gangouy@hunnu.edu.cn

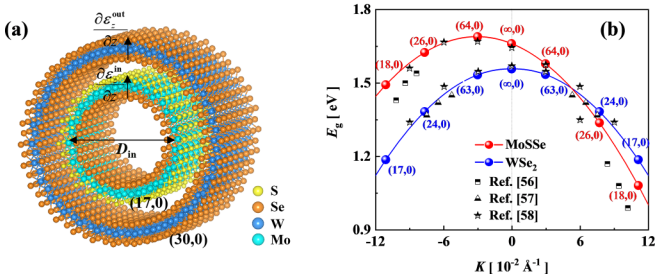

FIG. 1. (a) Schematic diagram of one-dimensional (1D) zigzag MoSSe/WSe_2 van der Waals (vdW) heterostructure. (b) The band gaps of zigzag MoSSe and WSe_2 nanotubes (NTs) as a function of curvature ($K = 1/R$) and chiral indices (n, m). The positive (negative) curvature corresponds to the S-out (Se-out) case in MoSSe NTs.

is beneficial for the collection of photogenerated carriers [18,26]. Therefore, combining the significant advantages of Janus TMDs and superior photoelectric conversion properties of 1D NTs to construct 1D vdW heterostructures may be an effective strategy to improve the efficiency of solar cells.

In this paper, we investigate the flexoelectric effect and electronegativity difference on the photoelectric conversion properties of 1D Janus-MoSSe/WSe_2 vdW heterostructures in terms of the atomic-bond-relaxation (ABR) method [27–29], Marcus theory [30,31], detailed balance principle (DBP) [32,33], and *ab initio* nonadiabatic molecular dynamics (NAMD) simulations. First, we address the size-dependent band offsets of MoSSe and WSe_2 NTs as well as determine the optimal stacking configuration and the type of band alignment. Second, we explore the effects of flexoelectricity and electronegativity difference on the photoelectric conversion properties and clarify the underlying mechanism of generation, separation, transfer, and collection of photoexcited carriers in a 1D system. Last, we optimize the diameter of 1D MoSSe/WSe_2 to achieve a maximum PCE which is much higher than those of 1D MoS_2/WSe_2- and 2D MoSSe/WSe_2-based models. Our findings provide an effective strategy to design high-efficiency 1D TMD-based solar cells.

II. THEORETICAL METHODOLOGIES

A. Curvature-induced band offset

Like the single-wall carbon NTs, single-wall TMD NTs can be treated as a TMD monolayer rolled up into a tube, and they can be classified as zigzag, armchair, and chiral NTs in terms of different chiral indices (n, m) [34,35]. Note that the chiral vector is defined within the transition-metal-atom plane. Therefore, for the TMD NTs with chiral indices (n, m), the radius of the transition metal layer is $R = a\sqrt{n^2 + nm + m^2}/2\pi$, and a is the lattice constant. Analogously, a 1D vdW heterostructure can be obtained by rolling up a 2D vdW heterostructure. In our case, we focus on the zigzag TMD NTs with chiral indices (n,0) due to their direct band gap characteristic. A kind of 1D radial vdW heterostructure constructed by zigzag MoSSe and WSe_2 NTs is shown in Fig. 1(a). The diameter of an inner (MoSSe) NT is represented by D_{in}, the chiral indices (n,0) of inner and outer NTs are (17,0) and (30,0), respectively. For the 1D MoSSe/WSe_2 vdW heterostructures, the total interaction energy can be expressed as the summation of the intralayer interaction energy of the inner NT ($E^{\text{in}}_{\text{intra}}$), intralayer interaction energy of the outer NT ($E^{\text{out}}_{\text{intra}}$), and the interlayer interaction energy (E_{inter}) induced by weak vdW force, i.e.,

$$E_{\text{total}} = E^{\text{in}}_{\text{intra}} + E^{\text{out}}_{\text{intra}} + E_{\text{inter}}. \tag{1}$$

It is worth noting that the intralayer interaction energy of a NT consists of Coulomb electrostatic energy, bond-stretching energy, and bond-angle-variation energy [36] (see Supplemental Material for more details [37]). The interlayer interaction induced by weak vdW force can be calculated by the Lennard-Jones model: $E_{\text{inter}} = -\sum_1^i \sum_1^j [\Gamma(\sigma/r_{ij})^{12} - (\sigma/r_{ij})^6]$, where Γ and σ are potential parameters, and r_{ij} denotes the distance between the ith atom in the outer NT and the jth atom in the inner NT. In a 1D vdW heterostructure, the bending-induced average strain is $\bar{\varepsilon} = \int_0^{H/2} \frac{2}{H} zKdz = H/2D$, where $K = 1/R$ is the curvature, H denotes the thickness of the 2D counterparts, D is the diameter of NTs, and z is taken along the radial direction of NT [19].

Indeed, a system will relax spontaneously to a new self-equilibrium state under external strain perturbation in terms of ABR consideration [27–29], resulting in some distinctive features owing to the changes of total interaction energy and the Hamiltonian. Physically, the single-body Hamiltonian can be expressed as $\hat{H} = \hat{H}_0 + \hat{H}' = -\frac{\hbar^2\nabla^2}{2m_e} + V_a(r) + V_{\text{cry}}(r + a)$, where m_e is the electron effective mass, $V_a(r)$ and $V_{\text{cry}}(r)$ denote the intra-atomic trapping potential and the periodic potential of the crystal [27]. In addition, the band-gap value of a specimen is proportional to the first Fourier coefficient of the potential energy function. Thus, the band gap is proportional to the single bond energy, i.e., $E_g = 2|V_1| = 2\int V_{\text{cry}}(r)e^{ikr} \propto \langle E_0 \rangle$, where $\langle E_0 \rangle$ denotes the average single bond energy. Consequently, the diameter-dependent band gap of the inner (outer) NT can be derived as

$$E_g^{\text{in(out)}}(D) = E_g^{1L}(1 + \Delta_{\text{intra}} + \Delta_{\text{inter}}), \tag{2}$$

where E_g^{1L} is the band gap of monolayer counterparts, $\Delta_{\text{intra}} = \Delta E_{\text{intra}}/NE_0^{1L}$ and $\Delta_{\text{inter}} = \Delta E_{\text{inter}}/2NE_0^{1L}$ denote the disturbance induced by bending-induced strain and weak vdW force; ΔE_{intra} (ΔE_{inter}) is the variation of intralayer (interlayer) interaction energy, and N and E_0^{1L} are the number of atoms and single bond energy.

B. Flexoelectricity and electronegativity

Generally, the polarization of 1D vdW heterostructures can be expressed as $P^Z = \mu_z(\partial\varepsilon_z^{\text{in}}/\partial z + \partial\varepsilon_z^{\text{out}}/\partial z) + \frac{1}{S}\sum_{i=1}^N q_i Z_i$; the previous and latter terms denote the polarization induced by the flexoelectric effect and electronegativity difference between S and Se in the Janus MoSSe structures, respectively [19,38]. Here, μ_z is the flexoelectric coefficient, $\partial\varepsilon_z^{\text{in}}/\partial z$ ($\partial\varepsilon_z^{\text{out}}/\partial z$) represents the strain gradient of the inner (outer) NT along the radial direction, S and q_i are the area and the

partial electrostatic charges for atoms i, and Z_i denotes the coordination numbers. Therefore, the diameter-dependent total electrostatic potential difference (i.e., the summation of flexoelectric and intrinsic potential difference: $\Delta\varphi_{\text{flex}} + \Delta\varphi_{\text{intri}}$) of 1D MoSSe/$WSe_2$ vdW heterostructures is

$$\Delta\varphi(D) = \frac{4\sqrt{3}q_i H^2 D\nu_\perp}{a^2\kappa_0\kappa_r(2D + H\nu_\parallel)(2D - H)} + (\varphi_S - \varphi_{Se}), \quad (3)$$

where $\nu_\perp$ and $\nu_\parallel$ represent the out-of-plane and in-plane Poisson's ratio of NTs, κ_0 and κ_r are the vacuum permittivity and relative permittivity of materials, and φ_S (φ_{Se}) is the intrinsic electrostatic potential of S (Se) atomic layer.

Furthermore, the polarization charge induced by the flexoelectric effect is $q\rho_{\text{flex}}W_{\text{flex}} = -u_z(1/D_{\text{in}} + 1/D_{\text{out}})$, where ρ_{flex} and W_{flex} are the flexoelectric charge density and the width of the charge distribution. In terms of the piezophototronics theory [39], the Fermi level of a system is $E_F = E_{F0} + q^2\rho_{\text{flex}}W_{\text{flex}}^2/2\kappa_0\kappa_r$, and E_{F0} denotes the Fermi level in the absence of the flexoelectric effect. Moreover, the shifts of the conduction band minimum (CBM) and valence band maximum (VBM) of the inner (outer) NT can be calculated by the effective-mass approximation [40], i.e., $\Delta E_{CBM}(D) = \hbar^2\pi^2/(2m_eD^2)$ and $\Delta E_{VBM}(D) = \hbar^2\pi^2/(2m_hD^2)$, where $\hbar$ and m_h are the reduced Planck constant and the hole effective mass. Thus, the diameter-dependent shifts of CBM and VBM of the inner (outer) NT with the flexoelectric effect can be derived as

$$\Delta E_{CBM}^{in(out)}(D) = \left(\Delta E_{total} - \Delta E_{intra}^{out(in)} - \frac{1}{2}\Delta E_{inter}\right) \times \frac{E_g^{1L}}{NE_0^{1L}}\frac{m_h}{m_e + m_h} + \frac{q^2\rho_{\text{flex}}W_{\text{flex}}^2}{\kappa_0\kappa_r}$$

$$\Delta E_{VBM}^{in(out)}(D) = \left(\Delta E_{total} - \Delta E_{intra}^{out(in)} - \frac{1}{2}\Delta E_{inter}\right) \times \frac{E_g^{1L}}{NE_0^{1L}}\frac{m_e}{m_e + m_h} + \frac{q^2\rho_{\text{flex}}W_{\text{flex}}^2}{\kappa_0\kappa_r}, \quad (4)$$

where ΔE_{total} represents the change in total energy.

C. Photoelectric conversion properties

Theoretically, the light absorptance of a heterostructure can be calculated by using the law of luminous flux conservation [41,42] (see Supplemental Material for more details [37]). Considering the effects of the flexoelectric and intrinsic electric fields on charge transfer, the thermodynamic driving force of photogenerated electron (hole) transfer can be written as $-\Delta G_{e(h)} = E_{C(V)BM}^D - E_{C(V)BM}^A + \Delta\varphi_{\text{flex}} + \Delta\varphi_{\text{intri}}$, where $E_{C(V)BM}^D$ ($E_{C(V)BM}^A$) is the energy of the C(V)BM of the electron donor (acceptor), and $E_{CBM} = \chi - \Delta E_{CBM}$, $E_{VBM} = IP - \Delta E_{VBM}$, where χ and IP are the electron affinity and ionization potential of flat TMD monolayer. In light of the Marcus theory [30,31], the size-dependent electron (hole) transfer rate of 1D vdW heterostructures can be written as

$$k_{e(h)}(D) = \frac{2\pi}{\hbar}\sum_{d_0}^{d_0+z}\{k_0\exp[-\gamma(d_0+z)]\}^2\frac{1}{\sqrt{4\pi\lambda k_B T}}\exp\left(-\frac{\left[\lambda + E_{C(V)BM}^D - E_{C(V)BM}^A + \Delta\varphi_{\text{flex}} + \Delta\varphi_{\text{intri}}\right]^2}{4\lambda k_B T}\right), \quad (5)$$

where d_0 is the interface distance, γ and k_B are the attenuation factor and Boltzmann constant, and λ and k_0 are the reorganization energy and the rate at close contact. Therefore, the electron (hole) collection efficiency in 1D vdW heterostructures is

$$F_{ce-e(h)}(D) = \frac{1}{1 + \{d_0/[2k_{e(h)}\tau_r(d_0+z)]\}\exp\left\{-\left[E_{C(V)BM}^D - E_{C(V)BM}^A\right]/k_BT\right\}}, \quad (6)$$

where τ_r is the radiative lifetime of photogenerated carriers [43].

In terms of the classic DBP proposed by Shockley and Queisser [32], we further consider the influence of the flexoelectric effect and electronegativity difference on the photoelectric properties (e.g., the short-circuit current density, open-circuit voltage, and PCE) of 1D vdW heterostructure solar cells (see Supplemental Material [37] for more details). According to Eqs. (5) and (6), (S4) and (S5) in the Supplemental Material [37], and $-\Delta G = E_g - E_{CT} + \Delta\varphi$, an analytical expression between open-circuit voltage (V_{oc}) and charge transfer state energy (E_{CT}) can be obtained as

$$V_{oc} = \frac{E_{CT}}{q} - \frac{k_BT_c}{q}\ln\left(\frac{J_r(SQ)\left\{C_{ET}\exp\left[\frac{(E_{CT}+\lambda-E_g-\Delta\varphi)^2+4\lambda E_{CT}}{4\lambda k_BT_c}\right]\right\} + \exp\left(\frac{-E_g+\Delta\varphi}{k_BT_c}\right)}{J_{ph}(SQ)}\right.$$
$$\left. + \frac{(R_L + R_{SHR})\left\{C_{ET}\exp\left[\frac{(E_{CT}+\lambda-E_g-\Delta\varphi)^2-4\lambda E_g}{4\lambda k_BT_c}\right] - \exp\left(\frac{-E_{CT}}{k_BT_c}\right)\right\}}{J_{ph}(SQ)}\right), \quad (7)$$

where $J_r(SQ)$ and $R_L + R_{SHR}$ represent the radiative and nonradiative recombination, R_L and R_{SHR} are the Coulomb-interacting Langevin recombination and trap-assisted Shockley-Read-Hall recombination, $J_{ph}(SQ)$ denotes the photocurrent density, and $C_{ET} = d_0\hbar\sqrt{\lambda k_BT_c}/(2\pi^{1/3}\tau_r(d_0+z)\{k_0\exp[-\gamma(d_0+z)]\}^2)$.

D. Computational methods

The structural relaxation and electronic properties of NTs are performed in the framework of density functional theory as implemented in VASP [44]. The NAMD calculations are performed using the Hefei-NAMD code [45–47], which augments VASP with the NAMD capabilities within the time-dependent Kohn-Sham theory and surface-hopping method based on classical path approximation [48,49]. The projector augmented-wave [50] pseudopotentials are used to describe the valence electron and core interactions. The generalized gradient approximation [51] in the Perdew-Burke-Ernzerhof [52] exchange-correlation functional is adopted. A plane-wave basis set with the kinetic energy cutoff $h^2|k+G|^2/2m = 500$eV is used for all calculations. The Brillouin zone integration is performed using a Γ-centered $1 \times 1 \times 6$ k-point mesh for the whole unit cell [53]. The convergence value for electronic relaxation between the sequential steps in the total energy calculations is $<10^{-5}$ eV, and the relaxation of the ions until the Hellmann-Feynman forces on each atom was <0.02 eV/Å. A vacuum spacing of ∼20 Å was set in the nonperiodic direction to prevent any unrealistic interactions between neighboring cells.

III. RESULTS AND DISCUSSION

A. Band offset and alignment

The structural stability of 1D MoSSe/WSe_2 vdW heterostructures can be explained by the formation energy and *ab initio* molecular dynamics simulations. The formation energy per unit cell of the heterostructure under $D_{in} = 17.4$ Å calculated by first principles is −0.86 eV, and the energy oscillates around a stable value (Fig. S1 in the Supplemental Material [37]), demonstrating the experimental possibilities and structural stability of 1D MoSSe/WSe_2 vdW heterostructures. Moreover, the stability of 1D TMD vdW heterostructures has been demonstrated thoroughly in previous experimental and theoretical studies [18,26,54,55]. Figure 1(b) presents the band-gap evolutions of MoSSe and WSe_2 NTs as a function of curvature. Obviously, the band gaps of WSe_2 NTs are symmetric with respect to the case of NTs in the $r \to \infty$ limit ($K = 0$), and the band gap increases with the decrease of curvature [i.e., increasing chiral indices (n, m)], and the limit is the band gap of the 2D counterpart. Interestingly, the band gaps of MoSSe NTs are asymmetric with respect to $K = 0$. This is mainly attributed to the broken out-of-plane symmetry of Janus structure in MoSSe NTs. In detail, we calculate the band structures of the (64,0) MoSSe NT under the conditions of negative, zero, and positive curvatures, as shown in Fig. S2 in the Supplemental Material [37]. Evidently, the band gap of the (64,0) MoSSe NT with negative curvature is larger than that of the planar MoSSe monolayer. Both for 2D MoSSe and the (64,0) MoSSe NT ($k = -0.03$ Å), the electron states near the CBM and VBM are from the contribution of Mo-d_{z^2} orbitals (Fig. S2 in the Supplemental Material [37]). The position of Mo-d_{z^2} shifts under the action of the flexoelectric field (Figs. S3(c) and S3(d) in the Supplemental Material [37]), resulting in a larger band gap of the MoSSe NT with $k = -0.03$ Å. It is well known that, for pristine TMDs such as WSe_2, both the deformation potential and the Stark effect

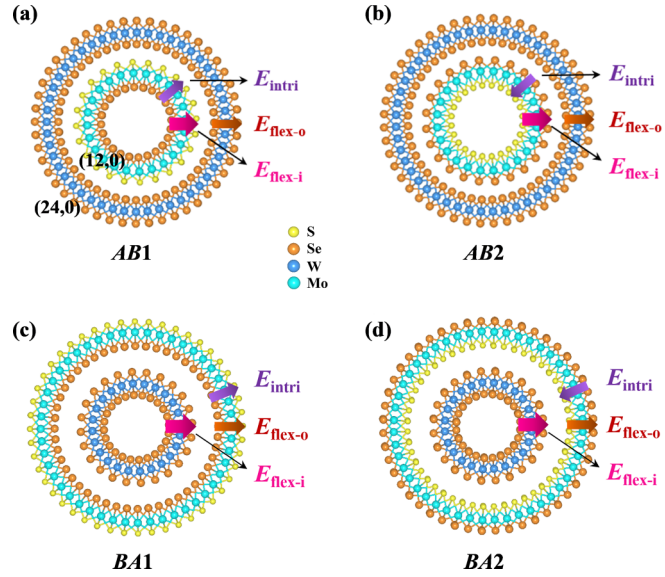

FIG. 2. (a)–(d) Schematics of four stacking configurations (*AB*1, *AB*2, *BA*1, and *BA*2), intrinsic electric field (purple arrows), flexoelectric field of outer nanotube (NT; brown arrows), and flexoelectric field of inner NT (magenta arrows) of one-dimensional (1D) MoSSe/WSe_2 van der Waals (vdW) heterostructures.

can lead to a monotonous band gap decrease with respect to the lattice strain and external electric field. However, for rolled Janus TMDs such as MoSSe, the joint effect of lattice strain, the intrinsic electric field, and the flexoelectric field will lead to an asymmetric and nonmonotonous decrease of the band gap [56]. In addition, we calculate the band structures of two zigzag NTs and find that they exhibit the direct band-gap characteristic (Fig. S4(a) in the Supplemental Material [37]), which makes them more favorable for photoelectric devices than armchair NTs with indirect band gaps. These results are in good agreement with previous reports [56–58].

Due to the unique intrinsic structure of Janus TMD NTs, the interfacial configuration of 1D TMD vdW heterostructures strongly correlates with the position and terminated surface of individual NTs. Here, four different stacking configurations, denoted as *AB*1, *AB*2, *BA*1, and *BA*2, are considered for 1D MoSSe/WSe_2 vdW heterostructures (Fig. 2). The most significant difference between the four stacking configurations is the direction of the electric field. Because of the electronegativity difference between S and Se in Janus MoSSe, the electrons are transferred from Se to S atom layers and an intrinsic electric field pointing from Se to S layer is induced [14,59]. Meanwhile, bending breaks the mirror symmetry and creates strain gradient and induces the flexoelectric field in the radial directions [19,56]. In *AB*1 and *BA*1 stacking configurations, the direction of the intrinsic electric field of the MoSSe NT is the same as that of the flexoelectric fields of inner and outer NTs, which is beneficial to the transfer of photogenerated carriers. For *AB*2 and *BA*2 stacking configurations, the opposite direction of the intrinsic electric field and the flexoelectric field will lead to very chaotic charge transfer, thereby suppressing the collection efficiency of electrons and holes. Similarly, Mogulkoc *et al.* [16] and Zheng *et al.* [59] demonstrated that the stacking configuration of Janus

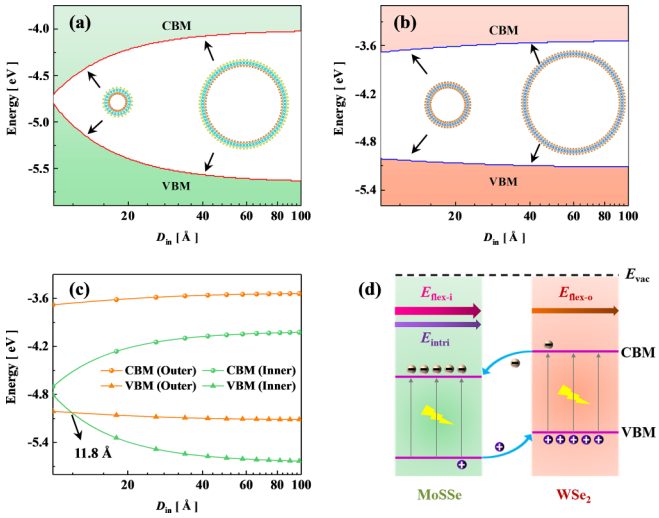

FIG. 3. Shifts of valence band maximum (VBM) and conduction band minimum (CBM) of (a) MoSSe nanotubes (NTs) and (b) WSe_2 NTs as a function of inner NT diameter in the case of *AB*1 stacking configuration. (c) Evolutions of band alignment of one-dimensional (1D) MoSSe/WSe_2 van der Waals (vdW) heterostructures with diameter. (d) Schematic representation of the type-II band alignment and photogenerated electron-hole pairs separation mechanism in 1D MoSSe/WSe_2 vdW heterostructures. The intertube distance is set to 3.44 Å.

TMD-based vdW heterostructures greatly influences charge transfer and photoelectric properties.

To explore the influence of band alignment on interfacial charge transfer and photoelectric properties, we calculate the diameter-dependent shifts of C(V)BM of inner and outer NTs in the case of the *AB*1 stacking configuration, as depicted in Figs. 3(a) and 3(b). For 1D Janus-MoSSe/WSe_2 vdW heterostructures, the intertube distance is ∼3.44 Å for all accessible diameter values in our case, which is consistent with the theoretical calculations and experimental measurements of double-wall TMD NTs [60,61]. Both for inner and outer NTs, the CBMs move up and VBMs move down as the inner NT diameter increases. As a result, the band alignment of 1D MoSSe/WSe_2 vdW heterostructures undergoes a transition from straddling type I to staggered type II, and the threshold size is 11.8 Å, which makes 1D MoSSe/WSe_2 vdW heterostructures applicable to light-emission and photovoltaic devices under different diameters [Fig. 3(c)]. This variation can be attributed the synergistic effect of diameter-dependent band-edge levels and curvature-induced flexoelectric. As the NT diameter increases, the CBMs and VBMs move up and down, respectively. Meanwhile, the Fermi energy level will shift under the action of the flexoelectric field, resulting in a shift of CBMs and VBMs, as indicated by Eq. (3) [39]. Similarly, Zhao *et al.* [62] showed that the combination of diameter-dependent band-edge levels, as well as the flexovoltage effect, can lead to a transition from type-II to type-I band alignment in 1D $MoSe_2/WS_2$, $MoTe_2/MoSe_2$, and $MoTe_2/WS_2$ vdW heterostructures. In detail, we draw the schematic representation of the staggered type-II band alignment and photogenerated electron-hole pairs separation mechanism of 1D MoSSe/WSe_2 vdW heterostructures with

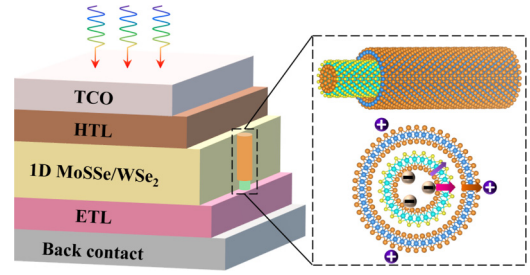

FIG. 4. Schematic illustration of one-dimensional (1D) MoSSe/WSe_2 van der Waals (vdW) heterostructure that is sandwiched between electron transport layer (ETL) and hole transport layer (HTL) for solar cell applications.

*AB*1 stacking configuration [Fig. 3(d)]. Owing to the effect of the flexoelectric field (E_{flex-o}) of the WSe_2 NT, the photogenerated electrons migrate to the heterostructure interface. Next, the electrons flow from the CBM of the Wse_2 NT to the CBM of the MoSSe NT under the action of the thermodynamic driving force of interfacial electron transfer. Finally, under the joint effect of the intrinsic electric field (E_{intri}) and the flexoelectric field (E_{flex-i}), the electrons migrate easily from the S atom plane to the Se atom plane of the Janus MoSSe NT. At the same time, the photogenerated holes flow from the VBM of the MoSSe NT to the VBM of the Wse_2 NT and finally accumulate on the outer surface of the 1D vdW heterostructures (right half of Fig. 4). In contrast, the intralayer recombination in traditional 2D heterostructures is relatively large due to the lack of the effects of the intrinsic electric and flexoelectric fields [6,8]. These results indicate that 1D MoSSe/Wse_2 vdW heterostructures have more efficient charge transfer and greater application potential than 2D heterostructures. From the band alignment and interfacial charge transfer of the *BA*1 stacking configuration (Fig. S5 in the Supplemental Material [37]), we concluded that the photogenerated electrons in the MoSSe NT and holes in the WSe_2 NT cannot be transferred smoothly due to the interfacial barrier. Therefore, we next focus on the photoelectric conversion properties of 1D MoSSe/WSe_2 vdW heterostructures in the case of the *AB*1 stacking mode.

B. Photoelectric conversion properties

Figure 4 exhibits the schematic illustration of the solar cell based on 1D MoSSe/WSe_2 vdW heterostructures. It contains an absorber layer composed of 1D MoSSe/WSe_2 heterostructures, which is sandwiched between the electron and hole transport layers. Generally, the photoelectric conversion properties of a solar cell strongly depend on the generation, separation, transfer, and collection of photoexcited electron-hole pairs. With the relation in Eq. (S3) in the Supplemental Material [37], we explore the diameter-dependent light absorptance of 1D MoSSe/WSe_2 vdW heterostructure solar cells in the visible light region [Fig. 5(a)]. Apparently, total light absorptance ($A_{abs}^{in} + A_{abs}^{out}$) of the system shows a trend of monotonous enhancement as the diameter of the NT decreases, and the maximum value approaches 88% when the diameter is <10 Å. These results can be attributed to the significant redshift of band gaps with increasing curvature

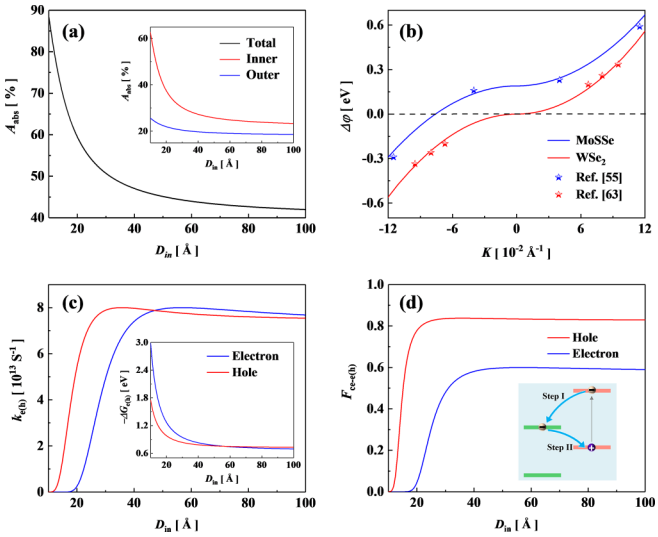

FIG. 5. (a) Nanotube (NT) diameter-dependent light absorptance of one-dimensional (1D) MoSSe/WSe_2 van der Waals (vdW) heterostructure solar cells. The inset is the variations of light absorption of inner and outer NTs (b) Evolutions of electrostatic potential difference as a function of the curvature for MoSSe and WSe_2 NTs. Diameter-dependent (c) electron (hole) transfer rate and (d) collection efficiency. The insets in (c) and (d) are the variation of electron (hole) transfer driving force with diameter and the schematic of two charge transfer processes in Marcus inverted region.

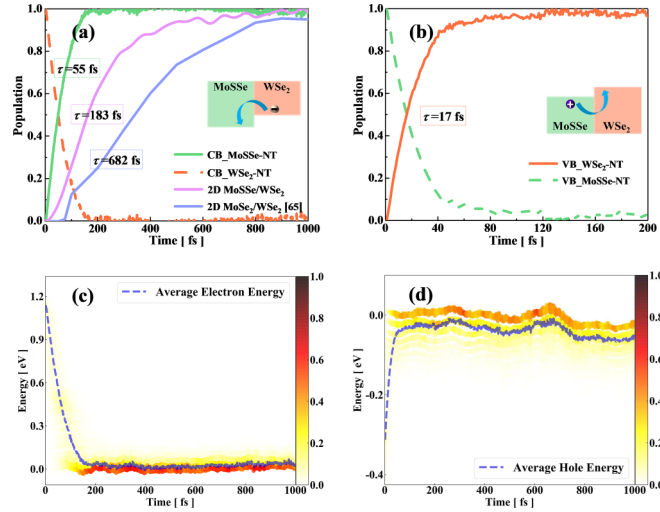

FIG. 6. Photogenerated carrier transfer dynamics in one-dimensional (1D) MoSSe/WSe_2 van der Waals (vdW) heterostructures. Time-dependent (a) and (b) populations and (c) and (d) energy evolutions of electron and hole; (a) and (c) for electron, (b) and (d) for hole.

and multiple internal reflections of incident light inside the heterostructure, resulting in a large number of photons with energy greater than or equal to the band gap being successfully captured in 1D heterostructures [17,26]. Moreover, since the band gap of the inner NT is smaller than that of the outer NT, the light-harvesting ability of the inner NT is greater than that of the outer NT [the inset in Fig. 5(a)].

Figure 5(b) displays the electrostatic potential difference of individual NTs in 1D MoSSe/WSe_2 heterostructures. It is obvious that the small-sized NTs exhibit a huge electrostatic potential difference, and the potential difference of the Janus MoSSe NT in the case of positive curvature is always more enormous than that of the WSe_2 NT due to the presence of the intrinsic electric field in Janus materials. These results are consistent with previous theoretical studies [55,63]. Figure 5(c) shows the diameter-dependent interfacial electron and hole transfer rates. We find that the charge transfer rates of the system can be up to $8 \times 10^{13} s^{-1}$ under the beneficial effects of the flexoelectric field, intrinsic electric field, and giant driving force [the inset of Fig. 5(c)]. Meanwhile, the electron and hole transfer rates increase sharply at the initial stage and then depress with increasing NT diameter, which is consistent with the Marcus-inverted charge transfer phenomena in related experimental measurements [31,64]. The schematic diagram of two charge transfer steps, namely, the dissociation of photogenerated electron-hole pairs and the recombination of carriers in the Marcus inverted region, are illustrated in Fig. 5(d). We clearly observe that the energy-wasting carrier recombination process occurs immediately after the dissociation process under an enormous driving force, thus resulting in a decrease of interfacial charge transfer rate. Furthermore, the electron (hole) collection efficiency of the 1D vdW heterostructure shows a similar trend to the electron (hole) transfer rate, and the electron and hole collection efficiencies increase to ~60 and 80%, respectively [Fig. 5(d)].

To gain in-depth insight into the effects of flexoelectricity and electronegativity difference on interfacial charge transfer, we further investigate the dynamic behaviors of photogenerated carrier transfer in Janus-MoSSe/WSe_2 systems based on NAMD simulations. Figures 6 and S6 in the Supplemental Material [37] show the dynamics of photogenerated carrier transfer and associated energy relaxation in 1D MoSSe/WSe_2 and 2D MoSSe/WSe_2 vdW heterostructures, respectively. It is evident from Fig. 6(a) that the process of electron transfer from the WSe_2 NT to the MoSSe NT is completed rapidly within 55 fs, which is much faster than those in 2D MoSSe/WSe_2 (183 fs, Fig. S6 in the Supplemental Material [37]), 2D $MoSe_2$/WSe_2 (682 fs) [65], and 2D MoS_2/WSe_2 (470 fs) [66] vdW heterostructures. The transfer times (τ) are fitted by the exponential relation: $f(t) = a + b\exp(-t/\tau)$. Such ultrafast interfacial charge transfer behavior is related to the polarization electric field induced by the flexoelectric effect of bent TMDs and electronegativity difference of Janus MoSSe. Theoretically, the electron (hole) transfer rate is proportional to $\exp(-\Delta E/k_B T)$, where the energy barrier (ΔE) can be given by the energy difference between the CBM or VBM of the donor and acceptor, i.e., $\Delta E = E^{A}_{C(V)BM} - E^{D}_{C(V)BM}$ [67]. Figure S7 in the Supplemental Material [37] displays the diameter-dependent energy barrier of electron transfer in the MoSSe/WSe_2 system. Obviously, the energy barrier gradually decreases as the diameter decreases. For the 1D MoSSe/WSe_2 vdW heterostructure, both the flexoelectric field induced by the flexoelectric effect and the intrinsic electric field induced by electronegativity difference will reduce the energy barrier (ΔE) of interfacial charge transfer, resulting in stronger interlayer coupling than the planar MoSSe/WSe_2 heterostructure [59,68]. Therefore, the 1D

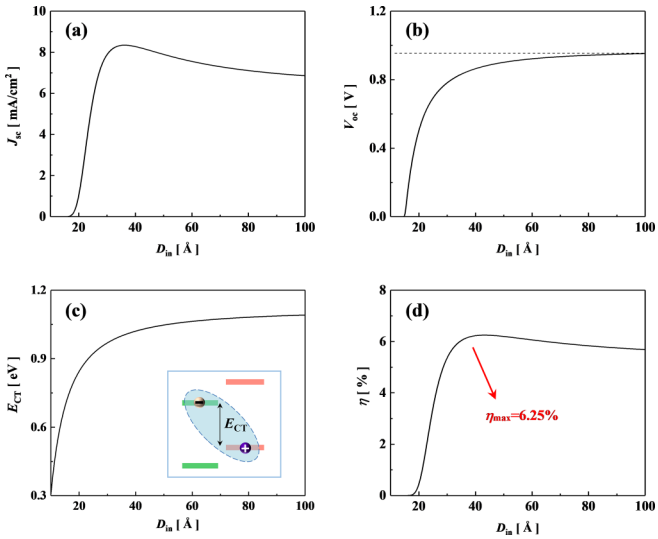

FIG. 7. Nanotube (NT) diameter-dependent photoelectric conversion properties of one-dimensional (1D) MoSSe/WSe_2 van der Waals (vdW) heterostructure solar cells. (a) Short-circuit current density (J_{sc}), (b) open-circuit voltage (V_{oc}). (c) Calculated charge transfer state energy (E_{CT}) vs NT diameter. The inset shows the schematic illustration of an interlayer charge transfer state with E_{CT}. (d) The evolution of the power conversion efficiency (PCE; η) with diameter.

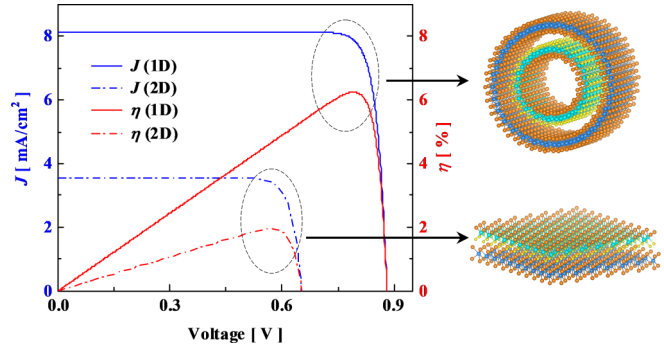

FIG. 8. $J-V$ and $\eta-V$ characteristics in one-dimensional (1D) MoSSe/WSe_2 and two-dimensional (2D) MoSSe/WSe_2 van der Waals (vdW) heterostructure solar cells.

MoSSe/WSe_2 vdW heterostructure shows faster interfacial electron transfer process compared with other 2D systems. In addition, the hole transfer process in 1D MoSSe/WSe_2 is relatively fast (17 fs), which can be demonstrated by the different average energy evolution of the corresponding energy states [Figs. 6(c) and 6(d)]. These features make 1D Janus TMD-based vdW heterostructures promising candidates for ultrafast photoelectric devices.

Considering the outstanding light-harvesting capability in the visible light region, ultrafast interfacial charge transfer, and excellent carrier collection efficiency of 1D MoSSe/WSe_2 vdW heterostructures, we further investigate the photoelectric conversion properties (e.g., the short-circuit current density, open-circuit voltage, and PCE) for exploiting these advantages in highly efficient solar cells. Figure 7(a) presents the short-circuit current density of a 1D MoSSe/WSe_2 vdW heterostructure-based solar cell as a function of NT diameter. It is evident that the short-circuit current density first gradually enhances and then reduces as NT diameter increases, and the maximum value is 8.34 mA/cm^2 which appears at 36.4 Å. This trend can be attributed to the Marcus-inverted charge transfer phenomena in the 1D MoSSe/WSe_2 system, where the charge transfer rate first increases and then decreases with increasing size [Fig. 5(c)]. Meanwhile, the open-circuit voltage increases monotonically with increasing size and finally reaches a saturation value [Fig. 7(b)]. The physical origin is that the open-circuit voltage of a solar cell is significantly affected by the charge transfer state energy, as indicated by Eq. (7). In fact, the charge transfer state energy (i.e., the energy difference between the CBM of the acceptor and the VBM of the donor) increases as the diameter of NTs increases [Fig. 7(c)], resulting in a change of open-circuit voltage. Therefore, in the regulation with different strategies, e.g., stacking mode, material selection, and external strains, the charge transfer state energy should be as large as possible to reduce the radiative and nonradiative energetic losses and obtain a higher open-circuit voltage [69,70]. Interestingly, the PCE of the 1D MoSSe/WSe_2 vdW heterostructure solar cell dramatically increases with increasing NT size and then decreases slightly as the diameter becomes 10 nm, and the optimal PCE can reach as high as 6.25% at 43.8 Å, as displayed in Fig. 7(d). This is mainly attributed to the strong light-matter interaction and ultrafast interfacial charge transfer in 1D MoSSe/WSe_2 vdW heterostructure solar cells.

C. J − V and η − V characteristics

Figure 8 shows the $J-V$ and $\eta-V$ characteristics of 1D and 2D MoSSe/WSe_2 vdW heterostructure solar cells under the standard test condition (i.e., AM 1.5 illumination). Obviously, the short-circuit current density and open-circuit voltage in a 2D MoSSe/WSe_2 vdW heterostructure are 3.56 mA/cm^2 and 0.65 V, and maximum PCE only reaches 1.94%. However, for the 1D MoSSe/WSe_2 heterostructure, the overall photoelectric conversion properties are significantly improved ($J_{sc} = 8.14\,\text{mA/cm}^2$, $V_{oc} = 0.88\,\text{V}$, $\eta_{max} = 6.25\%$), and the maximum PCE is boosted ~3.2 times that of its 2D planar counterparts. Such superior photoelectric properties of 1D MoSSe/WSe_2 vdW heterostructure solar cells are attributed to higher light absorptance and ultrafast interfacial charge transfer induced by the flexoelectric effect and electronegativity difference. Similarly, Ghosh *et al.* [26] reported a 1D MoS_2/WS_2 hetero-NT with superior photoelectric and photocatalytic properties and found a threefold improvement in the photocurrent compared with 2D planar heterostructure.

To highlight the role of the Janus layer, we compare the photoelectric properties of 1D MoS_2/WSe_2 and 1D MoSSe/WSe_2 vdW heterostructure solar cells (Fig. S8 in the Supplemental Material [37]). The calculated PCEs of 1D MoS_2/WSe_2 without the Janus component and 1D MoSSe/WSe_2 heterostructure solar cells are 5.45 and 6.25%, respectively. In detail, Fig. S9 in the Supplemental Material [37] summarizes the external quantum efficiencies of the three systems, and it is found that the order of external quantum efficiency values is $EQE_{1D-MoSSe/WSe_2} > EQE_{1D-MoS_2/WSe_2} > EQE_{2D-MoSSe/WSe_2}$. These results demonstrate that the

flexoelectric effect in 1D heterostructures and electronegativity difference in the Janus materials can enhance the photoelectric conversion properties of solar cells. Therefore, to achieve high-performance solar cells, it is a feasible strategy to integrate a 1D vdW heterostructure with a Janus TMD into the devices.

IV. CONCLUSION

To summarize, we investigate a solar cell model based on 1D MoSSe/WSe_2 vdW heterostructures and further explore the flexoelectric effect and electronegativity difference on the photoelectric conversion properties by using the ABR consideration, modified Marcus theory, modified DBP, and NAMD simulations. Our findings indicate that the 1D MoSSe/WSe_2 vdW heterostructure with *AB*1 stacking configuration exhibits ultrafast interfacial charge transfer due to the larger driving force induced by the flexoelectric effect and electronegativity difference. Specifically, the photogenerated electron (hole) transfer in the 1D MoSSe/WSe_2 system occurs quickly, within 55 (17) fs. Moreover, owing to excellent generation, separation, transfer, and collection of photoexcited electron-hole pairs, the system exhibits superior photoelectric conversion properties. Significantly, the optimal PCE of 1D MoSSe/WSe_2 vdW heterostructure solar cells can reach as high as 6.25% through modulating the NT diameter, which is considerably higher than that of 1D MoS_2/WSe_2 (5.45%) and 2D MoSSe/WSe_2 (1.94%) vdW heterostructure solar cells. In this paper, we demonstrate that introducing a 1D vdW heterostructure with Janus TMD materials is an effective strategy to improve the conversion efficiency of a solar cell. Our results rationalize the previous experimental results and provide a way to design high-performance 1D TMD-based solar cells.

ACKNOWLEDGMENT

This paper was supported by the National Natural Science Foundation of China (Grants No. U2001215 and No. 22203105).

[1] S. Manzeli, D. Ovchinnikov, D. Pasquier, O. V. Yazyev, and A. Kis, 2D transition metal dichalcogenides, Nat. Rev. Mater. **2**, 17033 (2017).

[2] P. V. Pham, S. C. Bodepudi, K. Shehzad, Y. Liu, Y. Xu, B. Yu, and X. Duan, 2D heterostructures for ubiquitous electronics and optoelectronics: Principles, opportunities, and challenges, Chem. Rev. **122**, 6514 (2022).

[3] E. Barré, O. Karni, E. Liu, A. L. O'Beirne, X. Chen, H. B. Ribeiro, L. Yu, B. Kim, K. Watanabe, T. Taniguchi *et al.*, Optical absorption of interlayer excitons in transition-metal dichalcogenide heterostructures, Science **376**, 406 (2022).

[4] K. F. Mak, C. Lee, J. Hone, J. Shan, and T. F. Heinz, Atomically Thin MoS_2: A New Direct-Gap Semiconductor, Phys. Rev. Lett. **105**, 136805 (2010).

[5] L. Britnell, R. M. Ribeiro, A. Eckmann, R. Jalil, B. D. Belle, A. Mishchenko, Y.-J. Kim, R. V. Gorbachev, T. Georgiou, S. V. Morozov *et al.*, Strong light-matter interactions in heterostructures of atomically thin films, Science **340**, 1311 (2013).

[6] C.-H. Lee, G.-H. Lee, A. M. van der Zande, W. Chen, Y. Li, M. Han, X. Cui, G. Arefe, C. Nuckolls, T. F. Heinz *et al.*, Atomically thin *p-n* junctions with van der Waals heterointerfaces, Nat. Nanotechnol. **9**, 676 (2014).

[7] N. Ubrig, E. Ponomarev, J. Zultak, D. Domaretskiy, V. Zólyomi, D. Terry, J. Howarth, I. Gutiérrez-Lezama, A. Zhukov, Z. R. Kudrynskyi *et al.*, Design of van der Waals interfaces for broad-spectrum optoelectronics, Nat. Mater. **19**, 299 (2020).

[8] H.-M. Li, D. Lee, D. Qu, X. Liu, J. Ryu, A. Seabaugh, and W. J. Yoo, Ultimate thin vertical *p–n* junction composed of two-dimensional layered molybdenum disulfide, Nat. Commun. **6**, 6564 (2015).

[9] M.-Y. Li, Y. Shi, C.-C. Cheng, L.-S. Lu, Y.-C. Lin, H.-L. Tang, M.-L. Tsai, C.-W. Chu, K.-H. Wei, J.-H. He *et al.*, Epitaxial growth of a monolayer WSe_2-MoS_2 lateral *p-n* junction with an atomically sharp interface, Science **349**, 524 (2015).

[10] J. Wong, D. Jariwala, G. Tagliabue, K. Tat, A. R. Davoyan, M. C. Sherrott, and H. A. Atwater, High photovoltaic quantum efficiency in ultrathin van der Waals heterostructures, ACS Nano **11**, 7230 (2017).

[11] E. McVay, A. Zubair, Y. Lin, A. Nourbakhsh, and T. Palacios, Impact of Al_2O_3 passivation on the photovoltaic performance of vertical WSe_2 Schottky junction solar cells, ACS Appl. Mater. Interfaces **12**, 57987 (2020).

[12] A.-Y. Lu, H. Zhu, J. Xiao, C.-P. Chuu, Y. Han, M.-H. Chiu, C.-C. Cheng, C.-W. Yang, K.-H. Wei, Y. Yang *et al.*, Janus monolayers of transition metal dichalcogenides, Nat. Nanotechnol. **12**, 744 (2017).

[13] J. Zhang, S. Jia, I. Kholmanov, L. Dong, D. Er, W. Chen, H. Guo, Z. Jin, V. B. Shenoy, L. Shi *et al.*, Janus monolayer transition-metal dichalcogenides, ACS Nano **11**, 8192 (2017).

[14] C. Xia, W. Xiong, J. Du, T. Wang, Y. Peng, and J. Li, Universality of electronic characteristics and photocatalyst applications in the two-dimensional Janus transition metal dichalcogenides, Phys. Rev. B **98**, 165424 (2018).

[15] K. Zhang, Y. Guo, Q. Ji, A.-Y. Lu, C. Su, H. Wang, A. A. Puretzky, D. B. Geohegan, X. Qian, S. Fang *et al.*, Enhancement of van der Waals interlayer coupling through polar Janus MoSSe, J. Am. Chem. Soc. **142**, 17499 (2020).

[16] Y. Mogulkoc, R. Caglayan, and Y. O. Ciftci, Band Alignment in Monolayer Boron Phosphide with Janus MoSSe Heterobilayers Under Strain and Electric Field, Phys. Rev. Appl. **16**, 024001 (2021).

[17] Y. J. Zhang, T. Ideue, M. Onga, F. Qin, R. Suzuki, A. Zak, R. Tenne, J. H. Smet, and Y. Iwasa, Enhanced intrinsic photovoltaic effect in tungsten disulfide nanotubes, Nature (London) **570**, 349 (2019).

[18] R. Xiang, T. Inoue, Y. Zheng, A. Kumamoto, Y. Qian, Y. Sato, M. Liu, D. Tang, D. Gokhale, J. Guo *et al.*, One-dimensional van der Waals heterostructures, Science **367**, 537 (2020).

[19] X. Zhuang, B. He, B. Javvaji, and H. S. Park, Intrinsic bending flexoelectric constants in two-dimensional materials, Phys. Rev. B **99**, 054105 (2019).

[20] J. Jiang, Z. Chen, Y. Hu, Y. Xiang, L. Zhang, Y. Wang, G.-C. Wang, and J. Shi, Flexo-photovoltaic effect in MoS_2, Nat. Nanotechnol. **16**, 894 (2021).

[21] P. Gentile, M. Cuoco, O. M. Volkov, Z.-J. Ying, I. J. Vera-Marun, D. Makarov, and C. Ortix, Electronic materials with nanoscale curved geometries, Nat. Electron. **5**, 551 (2022).

[22] M. G. Burdanova, R. J. Kashtiban, Y. Zheng, R. Xiang, S. Chiashi, J. M. Woolley, M. Staniforth, E. Sakamoto-Rablah, X. Xie, M. Broome *et al.*, Ultrafast optoelectronic processes in 1D radial van der Waals heterostructures: Carbon, boron nitride, and MoS_2 nanotubes with coexisting excitons and highly mobile charges, Nano Lett. **20**, 3560 (2020).

[23] M. G. Burdanova, M. Liu, M. Staniforth, Y. Zheng, R. Xiang, S. Chiashi, A. Anisimov, E. I. Kauppinen, S. Maruyama, and J. Lloyd-Hughes, Intertube excitonic coupling in nanotube van der Waals heterostructures, Adv. Funct. Mater. **32**, 2104969 (2021).

[24] B. Zhao, Z. Wan, Y. Liu, J. Xu, X. Yang, D. Shen, Z. Zhang, C. Guo, Q. Qian, J. Li *et al.*, High-order superlattices by rolling up van der Waals heterostructures, Nature (London) **591**, 385 (2021).

[25] S. Cambré, M. Liu, D. Levshov, K. Otsuka, S. Maruyama, and R. Xiang, Nanotube-based 1D heterostructures coupled by van der Waals forces, Small **17**, 2102585 (2021).

[26] R. Ghosh, M. Singh, L. W. Chang, H.-I. Lin, Y. S. Chen, J. Muthu, B. Papnai, Y. S. Kang, Y.-M. Liao, K. P. Bera *et al.*, Enhancing the photoelectrochemical hydrogen evolution reaction through nanoscrolling of two-dimensional material heterojunctions, ACS Nano **16**, 5743 (2022).

[27] C. Q. Sun, Size dependence of nanostructures: Impact of bond order deficiency, Prog. Solid State Chem. **35**, 1 (2007).

[28] G. Ouyang, C. X. Wang, and G. W. Yang, Surface energy of nanostructural materials with negative curvature and related size effects, Chem. Rev. **109**, 4221 (2009).

[29] A. Zhang, Z. Zhu, Y. He, and G. Ouyang, Structure stabilities and transitions in polyhedral metal nanocrystals: An atomic-bond relaxation approach, Appl. Phys. Lett. **100**, 171912 (2012).

[30] R. A. Marcus, On the theory of oxidation-reduction reactions involving electron transfer. I, J. Chem. Phys. **24**, 966 (1956).

[31] J. Wang, T. Ding, K. Gao, L. Wang, P. Zhou, and K. Wu, Marcus inverted region of charge transfer from low-dimensional semiconductor materials, Nat. Commun. **12**, 6333 (2021).

[32] W. Shockley and H. J. Queisser, Detailed balance limit of efficiency of *p-n* junction solar cells, J. Appl. Phys. **32**, 510 (1961).

[33] J. Dong, Y. Zhao, G. Ouyang, and G. Yang, A perspective on optimizing photoelectric conversion process in 2D transition-metal dichalcogenides and related heterostructures, Appl. Phys. Lett. **120**, 080501 (2022).

[34] G. Seifert, H. Terrones, M. Terrones, G. Jungnickel, and T. Frauenheim, Structure and Electronic Properties of MoS_2 Nanotubes, Phys. Rev. Lett. **85**, 146 (2000).

[35] A. E. G. Mikkelsen, F. T. Bölle, K. S. Thygesen, T. Vegge, and I. E. Castelli, Band structure of MoSTe Janus nanotubes, Phys. Rev. Mater. **5**, 014002 (2021).

[36] V. Varshney, S. S. Patnaik, C. Muratore, A. K. Roy, A. A. Voevodin, and B. L. Farmer, MD simulations of molybdenum disulphide (MoS_2): Force-field parameterization and thermal transport behavior, Comput. Mater. Sci. **48**, 101 (2010).

[37] See Supplemental Material at http://link.aps.org/supplemental/10.1103/PhysRevB.108.045416 for theoretical principles and computational details (bond identities and modified-DBP, calculations of the electronic properties, band alignment, photogenerated carrier transfer dynamics, external quantum efficiency, and characteristics). The Supplemental Material also contains Refs. [71–75].

[38] J. Zhang, On the piezopotential properties of two-dimensional materials, Nano Energy **58**, 568 (2019).

[39] Y. Zhang, Y. Liu, and Z. L. Wang, Fundamental theory of piezotronics, Adv. Mater. **23**, 3004 (2011).

[40] L. Brus, Electronic wave functions in semiconductor clusters: Experiment and theory, J. Phys. Chem. **90**, 2555 (1986).

[41] M. A. Green, Lambertian light trapping in textured solar cells and light-emitting diodes: Analytical solutions, Prog. Photovolt. **10**, 235 (2002).

[42] S. Mirabella, R. Agosta, G. Franzò, I. Crupi, M. Miritello, R. Lo Savio, M. A. Di Stefano, S. Di Marco, F. Simone, and A. Terrasi, Light absorption in silicon quantum dots embedded in silica, J. Appl. Phys. **106**, 103505 (2009).

[43] T. Kirchartz, J. Mattheis, and U. Rau, Detailed balance theory of excitonic and bulk heterojunction solar cells, Phys. Rev. B **78**, 235320 (2008).

[44] G. Kresse and J. Furthmüller, Efficiency of *ab-initio* total energy calculations for metals and semiconductors using a plane-wave basis set, Comput. Mater. Sci. **6**, 15 (1996).

[45] A. V. Akimov, A simple phase correction makes a big difference in nonadiabatic molecular dynamics, J. Phys. Chem. Lett. **9**, 6096 (2018).

[46] Q. Zheng, W. Chu, C. Zhao, L. Zhang, H. Guo, Y. Wang, X. Jiang, and J. Zhao, *Ab initio* nonadiabatic molecular dynamics investigations on the excited carriers in condensed matter systems, WIREs Comput. Mol. Sci. **9**, e1411 (2019).

[47] Y. Yin, X. Zhao, X. Ren, K. Liu, J. Zhao, L. Zhang, and S. Li, Thickness dependent ultrafast charge transfer in BP/MoS_2 heterostructure, Adv. Funct. Mater. **32**, 2206952 (2022).

[48] A. V. Akimov and O. V. Prezhdo, The PYXAID program for nonadiabatic molecular dynamics in condensed matter systems, J. Chem. Theory Comput. **9**, 4959 (2013).

[49] A. V. Akimov and O. V. Prezhdo, Advanced capabilities of the PYXAID program: Integration schemes, decoherence effects, multiexcitonic states, and field-matter interaction, J. Chem. Theory Comput. **10**, 789 (2014).

[50] P. E. Blöchl, Projector augmented-wave method, Phys. Rev. B **50**, 17953 (1994).

[51] J. P. Perdew, J. A. Chevary, S. H. Vosko, K. A. Jackson, M. R. Pederson, D. J. Singh, and C. Fiolhais, Atoms, molecules, solids, and surfaces: Applications of the generalized gradient approximation for exchange and correlation, Phys. Rev. B **46**, 6671 (1992).

[52] J. P. Perdew, K. Burke, and M. Ernzerhof, Generalized Gradient Approximation Made Simple, Phys. Rev. Lett. **77**, 3865 (1996).

[53] H. J. Monkhorst and J. D. Pack, Special points for Brillouin-zone integrations, Phys. Rev. B **13**, 5188 (1976).

[54] S. Xie, H. Jin, Y. Wei, and S. Wei, Theoretical investigation on stability and electronic properties of Janus MoSSe nanotubes for optoelectronic applications, Optik **227**, 166105 (2021).

[55] X. Wang, Y. Liu, J. Ren, K. Dou, X. Shi, and R. Zhang, A revised mechanism of band gap evolution of TMDC nanotubes and its application to Janus TMDC nanotubes: Negative electron and hole compressibility, J. Mater. Chem. C **9**, 8920 (2021).

[56] K. P. Dou, H. H. Hu, X. Wang, X. Wang, H. Jin, G.-P. Zhang, X.-Q. Shi, and L. Kou, Asymmetrically flexoelectric gating effect of Janus transition-metal dichalcogenides and their sensor applications, J. Mater. Chem. C **8**, 11457 (2020).

[57] Y. F. Luo, Y. Pang, M. Tang, Q. Song, and M. Wang, Electronic properties of Janus MoSSe nanotubes, Comput. Mater. Sci. **156**, 315 (2019).

[58] B.-L. Gao, S.-H. Ke, G. Song, J. Zhang, L. Zhou, G.-N. Li, F. Liang, Y. Wang, and C. Dang, Structural and electronic properties of zigzag and armchair WSe_2 nanotubes, J. Alloys Compd. **695**, 2751 (2017).

[59] T. Zheng, Y.-C. Lin, N. Rafizadeh, D. B. Geohegan, Z. Ni, K. Xiao, and H. Zhao, Janus monolayers for ultrafast and directional charge transfer in transition metal dichalcogenide heterostructures, ACS Nano **16**, 4197 (2022).

[60] G. Seifert, T. Kohler, and R. Tenne, Stability of metal chalcogenide nanotubes, J. Phys. Chem. B **106**, 2497 (2002).

[61] F. L. Deepak, A. Mayoral, A. J. Steveson, S. M. Rosales, D. A. Blomd, and M. J. Yacaman, Insights into the capping and structure of MoS_2 nanotubes as revealed by aberration-corrected STEM, Nanoscale **2**, 2286 (2010).

[62] S. Zhao, C. Yang, Z. Zhu, X. Yao, and W. Li, Curvature-controlled band alignment transition in 1D van der Waals heterostructures, npj Comput. Mater. **9**, 92 (2023).

[63] D. Bennett, Flexoelectric-like radial polarization of single-walled nanotubes from first-principles, Electron. Struct. **3**, 015001 (2021).

[64] G. A. Parada, Z. K. Goldsmith, S. Kolmar, B. Pettersson Rimgard, B. Q. Mercado, L. Hammarström, S. Hammes-Schiffer, and J. M. Mayer, Concerted proton-electron transfer reactions in the Marcus inverted region, Science **364**, 471 (2019).

[65] Q. Zheng, Y. Xie, Z. Lan, O. V. Prezhdo, W. A. Saidi, and J. Zhao, Phonon-coupled ultrafast interlayer charge oscillation at van der Waals heterostructure interfaces, Phys. Rev. B **97**, 205417 (2018).

[66] B. Peng, G. Yu, X. Liu, B. Liu, X. Liang, L. Bi, L. Deng, T. C. Sum, and K. P. Loh, Ultrafast charge transfer in MoS_2/WSe_2 *p-n* heterojunction, 2D Mater. **3**, 025020 (2016).

[67] R. Krause, S. Aeschlimann, M. Chávez-Cervantes, R. PereaCausin, S. Brem, E. Malic, S. Forti, F. Fabbri, C. Coletti, and I. Gierz, Microscopic Understanding of Ultrafast Charge Transfer in Van Der Waals Heterostructures, Phys. Rev. Lett. **127**, 276401 (2021).

[68] Y. Liu, J. Zhang, S. Meng, C. Yam, and T. Frauenheim, Electric field tunable ultrafast interlayer charge transfer in graphene/WS_2 heterostructure, Nano Lett. **21**, 4403 (2021).

[69] S. M. Menke, N. A. Ran, G. C. Bazan, and R. H. Friend, Understanding energy loss in organic solar cells: Toward a new efficiency regime, Joule **2**, 25 (2018).

[70] M. Azzouzi, J. Yan, T. Kirchartz, K. Liu, J. Wang, H. Wu, and J. Nelson, Nonradiative Energy Losses in Bulk-Heterojunction Organic Photovoltaics, Phys. Rev. X **8**, 031055 (2018).

[71] W.-J. Yin, B. Wen, G.-Z. Nie, X.-L. Wei, and L.-M. Liu, Tunable dipole and carrier mobility for a few layer Janus MoSSe structure, J. Mater. Chem. C **6**, 1693 (2018).

[72] J. Kang, S. Tongay, J. Zhou, J. B. Li, and J. Q. Wu, Band offsets and heterostructures of two-dimensional semiconductors, Appl. Phys. Lett. **102**, 012111 (2013).

[73] A. Ramasubramaniam, Large excitonic effects in monolayers of molybdenum and tungsten dichalcogenides, Phys. Rev. B **86**, 115409 (2012).

[74] W. Zhao, Y. Li, W. Duan, and F. Ding, Ultra-stable small diameter hybrid transition metal dichalcogenide nanotubes *X-M-Y* (X, Y = S, Se, Te; M = Mo, W, Nb, Ta): A computational study, Nanoscale **7**, 13586 (2015).

[75] C. Zhou, Y. Zhao, S. Raju, Y. Wang, Z. Lin, M. Chan, and Y. Chai, Carrier type control of WSe_2 field-effect transistors by thickness modulation and MoO_3 layer doping, Adv. Funct. Mater. **26**, 4223 (2016).